

Cell-Type Prototype-Informed Neural Network for Gene Expression Estimation from Pathology Images

Kazuya Nishimura^{1,3} Ryoma Bise² Shinnosuke Matsuo² Haruka Hirose³ Yasuhiro Kojima³
¹The University of Osaka, Japan ²Kyushu University ³National Cancer Center Japan
k.nishimura.d3c@osaka-u.ac.jp

Abstract

Estimating slide- and patch-level gene expression profiles from pathology images enables rapid and low-cost molecular analysis with broad clinical impact. Despite strong results, existing approaches treat gene expression as a mere slide- or spot-level signal and do not incorporate the fact that the measured expression arises from the aggregation of underlying cell-level expression. To explicitly introduce this missing cell-resolved guidance, we propose a Cell-type Prototype-informed Neural Network (CPNN) that leverages publicly available single-cell RNA-sequencing datasets. Since single-cell measurements are noisy and not paired with histology images, we first estimate cell-type prototypes—mean expression profiles that capture stable gene–gene co-variation patterns. CPNN then learns cell-type compositional weights directly from images and models the relationship between prototypes and observed bulk or spatial expression, providing a biologically grounded and structurally regularized prediction framework. We evaluate CPNN on three slide-level datasets and three patch-level spatial transcriptomics datasets. Across all settings, CPNN achieves the highest performance in terms of Spearman correlation. Moreover, by visualizing the inferred compositional weights, our framework provides interpretable insights into which cell types drive the predicted expression. Code is publicly available at <https://github.com/naivete5656/CPNN>.

1. Introduction

Estimating gene expression directly from pathology whole-slide images (WSIs) has emerged as a promising alternative to RNA sequencing, enabling large-scale molecular profiling at a fraction of the cost. This capability supports molecular subtype classification, personalized treatment stratification, and investigations into how histological morphology reflects underlying gene expression [2, 10, 34, 36, 49].

Existing methods infer gene expression at the popula-

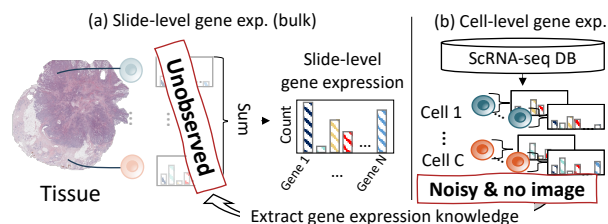


Figure 1. (a) Gene expression is observed together with histology image as the sum of unobserved cell-level expressions. Expression of individual cells is not directly measurable. (b) Cell-level gene expression profiles are obtained from a public single-cell RNA sequencing (scRNA-seq) database, which contains noisy measurements without corresponding image information.

tion level rather than at individual cells. Current approaches can be broadly categorized into two major settings. 1) Slide-level estimation which targets bulk transcriptomics, predicts expression aggregated over an entire tissue section. In this setting, multiple-instance learning architectures have been proposed to capture global tissue representations [2, 10, 34–36]. 2) Patch-level estimation which targets spatial transcriptomics, predicts expression in localized regions containing multiple cells. Models in this setting leverage both local and contextual features around each spatial spot using transformer or graph-convolution architectures [6, 13, 33, 45, 47].

While existing methods learn effective image features for the expression estimation, they do not explicitly model the underlying data-generation process in which the observed expression arises from the aggregation of cell-level signals. As shown in Figure 1(a), gene expression originates at the level of individual cells, but only the population-level aggregate is observed in slide- or patch-level measurements. Consequently, current approaches rely solely on these aggregated signals and cannot incorporate cell-resolved biological structure.

To address the lack of cell-level information, one natural direction is to leverage single-cell RNA-sequencing (scRNA-seq) data, which provide cell-level expression profiles for similar biological tissues. Such datasets are

publicly available and often annotated with cell types in databases such as GEO [4], SCPortalen [1], and the Single Cell Portal [37] (Figure 1(b)). However, they are noisy, affected by batch effects, and lack matched histopathology images, making their direct use for WSI-based gene expression estimation challenging.

To leverage single-cell information despite its noise and lack of correspondence with WSIs, we introduce a Cell-type Prototype-informed Neural Network (CPNN). The method assumes that slide- and patch-level gene expression can be represented as mixtures of cell-type gene expression profiles. CPNN estimates cell-type prototypes \bar{T} and compositional weights W , as illustrated in Figure 2. The predefined prototypes, derived from cell-level datasets, encode stable gene–gene covariation patterns for each cell type and serve as informative priors for estimation. During training, they are further refined to mitigate noise and reduce the modality gap between cell- and slide-level measurements.

We evaluate CPNN on three slide-level datasets (BRCA, KIRC, LUAD) and three patch-level spatial transcriptomics datasets (CSCC, Her2st, STNet). For patch-level prediction, CPNN can be integrated with existing architectures to fully leverage their feature extraction capabilities. Across all datasets, CPNN consistently achieves the highest Spearman correlation. In addition, visualizing the inferred compositional weights reveals which cell types drive the predictions, providing interpretable insights into the model’s decision process.

Our contributions are summarized as follows:

- A problem formulation for gene expression estimation from WSIs that leverages additional cell-level gene expression datasets retrieved from single-cell databases.
- A Cell-type Prototype-informed Neural Network (CPNN) that integrates cell-type prototypes and their compositional weights to predict gene expression.
- Comprehensive experiments on publicly available slide- and patch-level datasets demonstrating the superior performance and generalization ability of the our method.

2. Related work

Slide-Level Gene Expression Estimation. Slide-level gene expression estimation from whole slide images treated as a multiple-instance regression (AbReg) [10]. To reduce the overfitting problem, Schmauch et al. have reduced instances by clustering (HE2RNA) [35]. Alsafin et al. have introduced a transformer (tRNAformer) [2], and Pizurica et al. have introduced lineage operation (SEQUOIA VIS) [34] for gene expression estimation. Şenbabaoğlu et al. utilized patch-level representations derived from self-supervised learning, combined with an MLP, to estimate gene expression (MOSBY) [36]. However, the effectiveness of these modules has not been rigorously compared with the MIL methods on fair benchmarking.

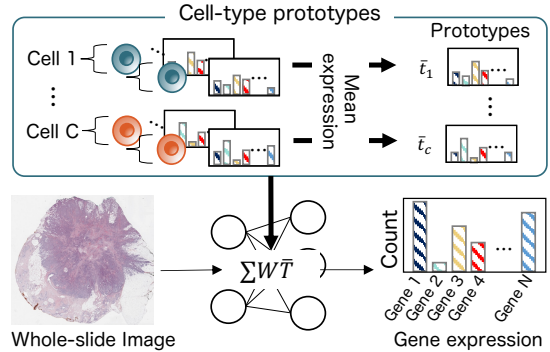


Figure 2. Illustration of concept of Cell-type Prototype-informed Neural Network (CPNN). We estimate gene expression based on cell-type prototypes by modeling the relationship between observed gene expression and cell-level gene expression.

Patch-Level Gene Expression Estimation. The emergence of spatial transcriptomics has stimulated the development of methods that infer gene expression directly from localized image patches [6, 7, 9, 13, 16, 33, 43, 45, 47]. Following the pioneering convolutional neural network (CNN)-based approach STNet introduced by [13], researchers have extended this line of work by incorporating graph neural networks (GNNs) [9, 16, 47] and transformer architectures such as TRIPLEX [6] to better capture spatial and contextual relationships among tissue regions. Another line of research aims to utilize retrieved gene expression to estimate expression profiles, as demonstrated by models such as BLEEP [43] and EGN [45], as well as HAGE [7]. While these retrieval-guided methods can help the model produce predictions that better approximate real observations, accurate alignment between image and gene expression remains difficult. These methods can not resolve the challenges of lack of cell-level information.

In contrast, our method complements the lack of cell-level information by introducing cell-level gene expression retrieved from database.

Single-Cell Deconvolution. Single-cell deconvolution, which infers the cell-type composition of slide- and patch-level expression using a single-cell dataset, has been proposed [5, 11, 22, 40]. These methods model the relationship between the mean gene expression for each cell type and the gene expression and estimate the cellular composition that reconstructs the slide-level gene expression.

This work, for the first time, leverages the relationship between target gene expression and cell-type prototypes to estimate slide- or patch-level gene expression, differing fundamentally from deconvolution-based approaches.

Physics-Informed Neural Network. A physics-informed neural network is a technique that integrates physical laws and data-driven representation of neural network [38]. The technique is widely used for various application fields such as imaging [19], super-resolution [46], and biomedicine

Table 1. Comparison of bulk, single-cell, and spatial transcriptomics techniques.

Techniques	Bulk	Single-cell	Spatial
With image	✓	✗	✓
Exp. resolution	Tissue	Single-cell	Spot
Number of samples	High	Moderate	Low
Cost per sample	Low	Medium	High

[17]. These methods enable the network to estimate regularized estimation via loss functions or model architectures with a small amount of training data. Our approach is similar to PINN in that it integrates gene expression with cell-level guidance based on physical relationships.

Multiple-Instance Learning. Multiple-instance learning is the task that estimates bag-level objectives from multiple instances (*i.e.*, a set of images) [14, 39, 42]. Research trends focus on efficiently aggregating features from multiple instances to generate bag features. Early methods relied on traditional approaches such as max pooling and mean pooling (Max and Mean) [39]. Attention mechanisms (AbMIL) [14] and transformers (ILRA) [42] have been introduced for more smart instance feature aggregation. A recent trend focuses on leveraging state space model to capture global contextual features, enabling more comprehensive representations (S4MIL, MambaMIL, SDMamba) [8, 44, 48].

Sequencing Techniques of RNA. RNA sequencing provides a comprehensive profile of RNA transcripts (*i.e.*, gene expression) and is essential for examining cellular function. There are some techniques, including bulk, single-cell, and spatial transcriptomics, each with distinct trade-offs in data scale, resolution, cost, and complexity. Table 1 shows a summary of the trade-off of each modality.

- Bulk transcriptomics (*i.e.*, slide-level gene expression) [31] provides the gene expression level across the cells in each biological specimen. It is relatively low cost, noise is less than other techniques, and there is a large-scale database that contains paired whole slide images and gene expression. However, it cannot capture cell-level activity.
- Single-cell transcriptomics [18] capture the gene expression of individual cells. However, it lacks corresponding imaging data, loses spatial context within tissues, and is more susceptible to noise.
- Spatial transcriptomic (*i.e.*, patch-level gene expression) [30] was developed to capture gene expression with spatial context and image. Although it can capture spatial context, spatial transcriptomics remains technically demanding and generally more costly.

3. Cell-Type Prototype-Informed Neural Network

In this section, we introduce our approach for modeling slide-level gene expression (Section 3.1). The same frame-

work can also be applied to patch-level estimation by replacing the whole-slide image with patch images, as described in Section 3.2.

3.1. Slide-Level Estimation

The goal of slide-level gene expression estimation is to estimate slide-level gene expression profiles from whole-slide pathology images. Given the n -th pathology whole-slide image $\mathcal{X}^{(n)} = \{\mathbf{x}_i^{(n)}\}_{i=1}^{N_p}$, where each $\mathbf{x}_i^{(n)}$ is a patch image, we aim to predict the slide-level gene expression vector $\mathbf{e}^{b(n)} \in \mathbb{R}^{N_{ge}}$, where each element corresponds to the expression count of a gene. N_p and N_{ge} denote the number of patches and genes. To regularize training, we incorporate cell-level expression dataset (single-cell RNA-seq.) from public sources, denoted as $\mathcal{G}_c = \{\mathbf{e}_c^{sc(k)}\}_{k=1}^{N_{sc}}$, where $\mathbf{e}_c^{sc(k)}$ is a k -th single-cell-level gene expression of the cell type c . N_{sc} is the number of single-cell samples of c .

An overview of the proposed method is shown in Figure 3. We assume that the expression level of each patch is an aggregation of cell-level expression across the patch and define slide-level expression using the gene expression prototype \bar{T} obtained from the obtained cell-level dataset and its compositional weight (Section 3.1.1). First, we generate the gene expression prototype \bar{T} from the cell-level dataset (Section 3.1.2). The compositional weight w is estimated from the patch cropped from the slide $\mathcal{X}^{(n)}$ (Section 3.1.3). We optimize our model with a negative log-likelihood for a slide-level gene expression and regularization (Section 3.1.4).

3.1.1. Formulation of Slide-Level Expression

We model the mean gene expression $\mu_g^b(\mathcal{X}^{(n)})$ as an aggregation of cell-type-specific prototypes with composition weights for the prototypes:

$$\mu_g^b(\mathcal{X}^{(n)}) = \underbrace{\alpha_g}_{\text{Tech. effect}} \sum_i \sum_c \overbrace{w(\mathbf{x}_i^{(n)})_c}^{\text{Comp. weights}} \underbrace{\bar{T}_{c,g}}_{\text{Prototypes}} + \underbrace{\beta_g}_{\text{Tech. effect}}, \quad (1)$$

where α_g represents a gene-specific scaling factor, which is expected to reflect the technical capturing rate of the corresponding gene, and β_g is a shift parameter due to the gap of modality for the gene g .

The total count of genes in the sample $l^{(n)}$ depends on factors that are difficult to estimate from the slide, such as tissue thickness. Therefore, our model estimates mean gene expression that is independent of the total count of the sample and achieves robustness for these factors.

In order to make our model estimates independent of the total counts across genes, We divid the $\mu^b(\mathcal{X}^{(n)})$ by the summation of it across genes and multiplied the actual total

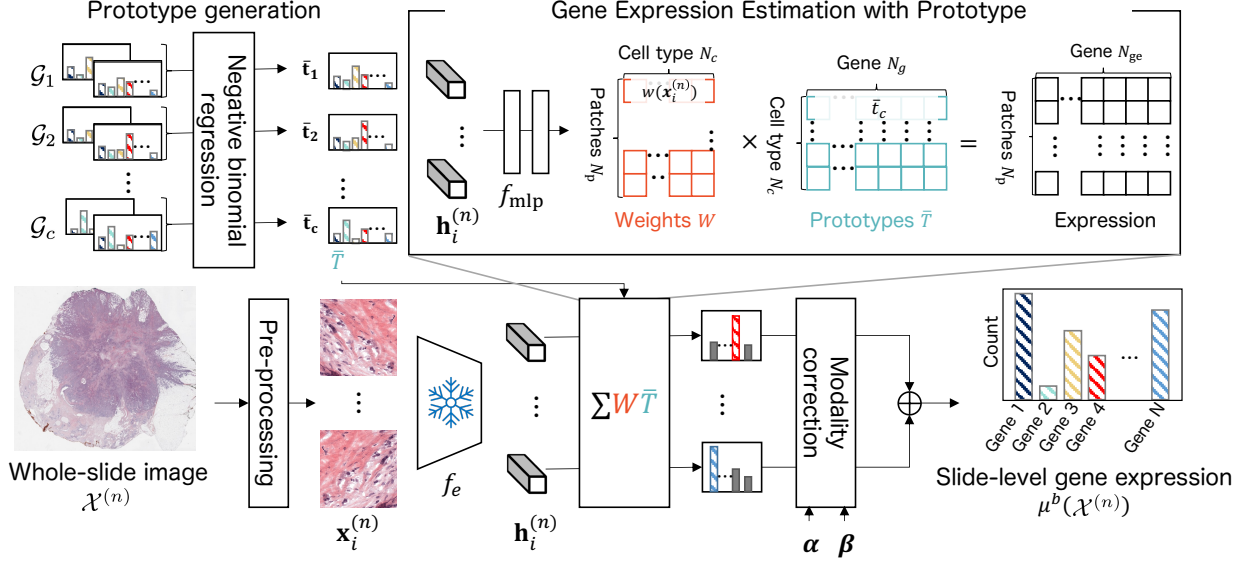


Figure 3. Overview of our method. Gene expression is estimated based on cell-type prototype \bar{T} and weight $w(\mathbf{x}_i^{(n)})$. The prototype supports the integration of covariance of gene expression among cells.

count of the sample n , which is $l^{(n)}$,

$$\bar{\mu}_g^b(\mathcal{X}^{(n)}) = l^{(n)} \frac{\mu_g^b(\mathcal{X}^{(n)})}{\sum_g \mu_g^b(\mathcal{X}^{(n)})}. \quad (2)$$

Similar to previous studies [25], we assume that the observed slide-level gene expression $e^{b(n)}$ follows a Negative Binomial distribution. The conditional probability of $e^{b(n)}$ given the slide $\mathcal{X}^{(n)}$ can be formulated as follows:

$$\Pr(e^{b(n)} | \mathcal{X}^{(n)}) = \prod_g \Pr(e_g^{b(n)} | \mathcal{X}^{(n)}), \quad (3)$$

$$\Pr(e_g^{b(n)} | \mathcal{X}^{(n)}) = \text{NB}(\bar{\mu}_g^b(\mathcal{X}^{(n)}), \theta_g^b), \quad (4)$$

where NB denotes the Negative Binomial distribution, $\bar{\mu}_g^b(\mathcal{X}^{(n)})$ represents the mean expression level of gene g computed using Eq. 2, and θ_g^b is the dispersion parameter for gene g .

3.1.2. Batch-Agnostic Prototype Generation

We first estimate gene expression prototypes \bar{T} from the cell-level dataset \mathcal{G}_c using negative binomial regression. Since single-cell data tend to contain an experimental batch effect (*i.e.*, a gap or shift due to a technical factor) between observed samples, we generate prototypes to estimate normalized gene expression using the negative binomial regression model [21].

We assume that the observed cell-level gene expression count follows a Negative Binomial distribution.

$$e_{c,g}^{sc(k)} \sim \text{NB}(\mu_{c,g}^{sc}, \theta_{c,g}^{sc}). \quad (5)$$

We model $\mu_{c,g}^{sc}$ using technical effects and the mean expression for each cell type t^{sc_c} .

$$\mu_{c,g}^{sc} = (t_{c,g} + b_d) s_d, \quad (6)$$

where s_d is a scaling parameter between the experimental condition d , and b_d is an additive gene-wise background shift of d . The prototype for each cell type $\mathbf{t}_c \in \mathbb{R}^{N_{ge}}$ is obtained by fitting observed gene expression with the regression model. The estimated prototype is normalized by $\bar{\mathbf{t}}_c = \frac{\mathbf{t}_c}{\sum_g \mathbf{t}_c}$, and $\bar{T} = [\bar{\mathbf{t}}_{1\top}, \dots, \bar{\mathbf{t}}_{N_{sc}\top}]^\top$ is obtained.

3.1.3. Gene Expression Estimation with Prototype

Next, we estimate the compositional weight for prototypes from the whole-slide image $\mathcal{X}^{(n)}$. Given the slide $\mathcal{X}^{(n)}$, we extract image features $\mathbf{h}_i^{(n)}$ for each patches $\mathbf{x}_i^{(n)}$ that is cropped from $\mathcal{X}^{(n)}$. We follow the pre-processing paradigm of MIL [28], which crops small patches from tissue regions and extracts the feature by an off-the-shelf image encoder f_e . The image feature $\mathbf{h}_i^{(n)} = f_e(\mathbf{x}_i^{(n)})$ is extracted from each patch $\mathbf{x}_i^{(n)}$. The weight is estimated from the extracted features $\mathbf{h}_i^{(n)}$ by the two linear layers f_{mlp} . Cell-type proportion for patch is obtained $w(x_i^{(n)}) = \text{softmax}(f_{mlp}(\mathbf{h}_i^{(n)}))$. As shown in Figure 3 of CPNN, the gene expression estimation is calculated by the dot product of the compositional weight and cell-type prototype \bar{T} . Gene expression for each patch is computed.

Cell-level and slide-level expression often exhibit gene-specific shifts and biases due to differences in measurement technology between these two modalities. To address these

discrepancies, we introduce α and β as scale and bias corrections. As shown in Equation 1, we derive bulk gene expression by applying these correction parameters to the gene expression obtained from the matrix product. Finally, the mean parameter $\bar{\mu}^b(\mathcal{X}^{(n)})$ of Negative Binomial Distribution is obtained by Equation 1 and 2.

3.1.4. Optimization

The main objective of our optimization is to reconstruct gene expression data. If only reconstruction loss is used for optimization, there is no grounding for prototype and proportions, and the optimization may lose the cell-level information. To avoid this issue, We impose a soft consistency constraint with the deconvolution results [21]. Our optimization updates θ^b , α , β , \bar{T} , and $w(\mathbf{x}_i^{(n)})$. To update $w(\mathbf{x}_i^{(n)})$, the parameter of neural network f_{mlp} is updated.

The total loss function of our method is as follows:

$$L_{\text{total}} = L_{\text{NB}} + \lambda L_{\text{R}}, \quad (7)$$

where the first term is the negative log-likelihood of assumed Negative Binomial distribution NB ($\bar{\mu}_g^b(\mathcal{X}^{(n)})$, θ_g^b) in Equation 4, and the second term is the regularization term, which softly takes consistency between single-cell deconvolution results. The λ is hyperparameter.

$$L_{\text{NB}}(\mathbf{E}^b, \bar{\mu}^b, \theta^b) = -\frac{1}{N_m} \sum_{n=1}^{N_m} \sum_{g=1}^{N_{\text{ge}}} \log \Pr(e_g^{b(n)} | \mathcal{X}^{(n)}),$$

where $\mathbf{E}^b = \{e^{b(n)}\}_{n=1}^{N_m}$, $\bar{\mu}^b = \{\bar{\mu}^b(\mathcal{X}^{(n)})\}_{n=1}^{N_m}$, $\theta^b = [\theta_g^b]_{g=1}^{N_{\text{ge}}}$ represent dispersion parameter of Negative Binomial distribution, N_m denotes the number of the slide in mini-batch. See Supplementary Material 7 for the detailed expression of L_{NB}

For the regularization term, we take consistency between the cell-type prototype and proportion.

$$L_{\text{R}}(\bar{T}^0, \bar{T}, \mathbf{W}, \bar{\mathbf{W}}) = \|\bar{T}^0 - \bar{T}\|^2 + \mathbb{E}_n \left[\left\| \mathbf{W}^{(n)} - \bar{\mathbf{W}}^{(n)} \right\|^2 \right], \quad (8)$$

where $\mathbf{W}^{(n)}$ denotes the compositional cell-type proportion for the n -th sample estimated by deconvolution method [21], and $\bar{\mathbf{W}}^{(n)} = \frac{1}{N_p} \sum_i w(\mathbf{x}_i^{(n)})$ represents the mean estimated weight, and \bar{T}^0 denotes the initial cell-type prototypes. Our method adjusts the prototype and proportions in a data-driven manner to optimize the reconstruction objective and achieves the estimation of slide-level gene expression with cell-level information.

3.2. Extension to Patch-Level Estimation

In spatial transcriptomics (ST), the goal of gene expression estimation is to predict expression levels for each patch image. Our proposed CPNN framework can be adapted to this

task because it aggregates patch-level predictions to infer the slide-level expression. The main modification lies in the loss function: since the observed ST data tend to be noisy and unstable, we replace the negative binomial loss, which depends on the absolute expression value, L_{NB} with a Pearson correlation-based loss, which focus on the relative relationships among patches.

For each patch image $\mathbf{x}_i^{(n)}$, the expression is estimated using cell-level prototypes derived following the procedure described in Section 3.1.1: $\hat{e}_{g,i}^{\text{st}(n)} = \alpha_g \sum_c w(\mathbf{x}_i^{(n)})_c \bar{T}_{c,g} + \beta_g$, where $\hat{e}_{g,i}^{\text{st}(n)}$ denotes the predicted expression of gene g for the patch. The model parameters are optimized by minimizing the Pearson correlation coefficient (PCC) loss between the predicted and observed expression across all genes with regularization loss for only prototype. In addition, by leveraging an existing module for estimating w , the framework can be seamlessly integrated as a plug-in component within existing analysis pipelines.

4. Experiments

We validate the effectiveness of our method in both slide- and patch-level settings.

Evaluation Metrics. Since the scaling bias of the sequencing technique can cause fluctuations in the absolute gene expression values, we used the Pearson and Spearman correlation coefficients (PCC, SCC) for the evaluation metrics. This metric was chosen to consider practical applications like Differentially Expressed Genes analysis [27], which analyzes the relative expression difference between samples as the downstream task.

4.1. Evaluation on Slide-Level Estimation

Experimental Setup. We used CLAM implementation [28] for MIL-based preprocessing to make a patch and CONCH [29] for the image encoder f_{t} . For the f_{mlp} , we adopt the projector architecture of LLaVA 1.5 [24]. For the Negative Binomial Regression and deconvolution, we used the implementation of cell2location [21] with default parameters. We trained our method using the AdamW optimizer [26] with a mini-batch size of 16 for 500 epochs. Early stopping was applied based on validation loss, using a validation set containing 30 patients. The learning rate was set to 1×10^{-3} and the regularization coefficient λ to 1×10^3 . For each dataset, we performed 4-fold cross-validation

Datasets: To evaluate the effectiveness of the proposed method, we validated our approach using three publicly available datasets from TCGA: BRCA, KIRC, and LUAD. Details of preprocessing for both slide-level and cell-level datasets are provided in Supplementary Material 8. An overview of each dataset is summarized below. **BRCA:** We collected 1,474 paired samples of whole-slide images (WSIs) and bulk gene expression profiles from TCGA-

Table 2. Comparison performance of slide-level gene expression estimation on TCGA-BRCA, KIRC, and LUAD. MIL: multiple instance learning, MIR: multiple instance regression, PCC: Pearson correlation coefficient, and SCC: spearman correlation coefficient

	Method	References	BRCA		KIRC		LUAD	
			PCC	SCC	PCC	SCC	PCC	SCC
MIL	Max [39]	Pattern Recog. 2018	0.219	0.225	0.162	0.161	0.170	0.173
	Mean [39]	Pattern Recog. 2018	0.247	0.263	0.211	0.217	0.203	0.213
	AbMIL [14]	ICML 2018	0.280	0.310	0.258	0.260	0.261	0.270
	ILRA [42]	ICLR 2023	0.291	0.310	0.261	0.276	0.245	0.283
	S4MIL [8]	MICCAI2023	0.292	0.301	0.225	0.231	0.243	0.252
	MambaMIL [44]	MICCAI 2024	0.293	0.309	0.212	0.224	0.280	0.284
	SRMambaMIL [44]	MICCAI 2024	0.304	0.311	0.244	0.251	0.276	0.286
	2DMamba [48]	CVPR2025	0.276	0.286	0.219	0.229	0.249	0.251
MIR	HE2RNA [35]	Nat. Commun. 2020	0.280	0.298	0.274	0.292	0.267	0.285
	AbReg [10]	MICCAIW 2022	0.267	0.273	0.242	0.244	0.243	0.251
	tRNAformer [2]	Commun. Biol. 2022	0.291	0.302	0.283	0.291	0.262	0.282
	MOSBY [36]	Sci. Rep. 2024	0.286	0.314	0.241	0.271	0.259	0.274
	SEQUOIA VIS [34]	Nat. Commun. 2024	0.285	0.295	0.267	0.272	0.252	0.258
	Ours	-	0.304	0.338	0.291	0.318	0.271	0.304

BRCA. For the single-cell dataset, 77,839 cells were obtained from [41]. Cell-type annotations were assigned to clusters based on known marker gene expression, resulting in 49 cell types. A total of 14,047 genes shared between the bulk and single-cell datasets were used for gene expression estimation. **KIRC:** We collected 681 paired samples from TCGA-KIRC. A total of 265,825 cells were obtained from the RCC single-cell dataset [23]. Cell-type labels (106 types) were assigned following the same procedure as BRCA. We selected 14,300 genes common to both datasets for downstream estimation. **LUAD:** We collected 756 paired samples from TCGA-LUAD. For the single-cell data, 171,128 cells were obtained from [20]. In total, 49 cell types were annotated. A set of 14,520 genes shared by the bulk and single-cell datasets was used for estimation.

Comparisons on Slide-Level Estimation. To evaluate the effectiveness of the proposed method, we compared it with thirteen existing approaches, including multiple-instance learning (MIL) and multiple-instance regression (MIR) methods. MIL baselines include pooling-based models (**Max**, **Mean** [39]), attention-based models (**AbMIL**, **ILRA**), and recent state-space models (**S4MIL** [8], **MambaMIL**, **SRMambaMIL** [44], **2DMamba** [48]). For MIR, we included transformer- and clustering-based methods such as **HE2RNA** [35], **AbReg** [10], **tRNAformer** [2], **MOSBY** [36], and **SEQUOIA VIS** [34]. All models used the same feature extractor (CONCH) and identical training settings for fair comparison.

Table 2 summarizes the overall results. Our proposed method achieves state-of-the-art (SOTA) performance on the SCC metric across all datasets. For the PCC metric, it

attains the best performance on BRCA and KIRC and ranks third on LUAD.

Among MIL-based approaches, transformer- and state-space-based models such as ILRA, S4MIL, and MambaMIL outperform conventional pooling methods (Max, Mean), indicating that attention-like mechanisms capture long-range contextual dependencies more effectively. However, even with these advanced aggregators, the performance gains remain limited.

For MIR-based methods, models specifically designed for regression—such as HE2RNA and tRNAformer—achieve slightly higher correlations than MIL-based approaches, particularly on the KIRC and LUAD datasets. These models benefit from instance selection and transformer-based feature learning. Nevertheless, estimating high-dimensional gene expression remains challenging without appropriate regularization.

Our proposed method achieved the highest overall performance across all datasets. These results demonstrate that our prototype-guided framework effectively supports high-dimensional gene expression estimation. Because each pre-defined prototype provide stable gene–gene covariation patterns, it serves as an implicit regularizer within the prediction space. Importantly, the ability to leverage cell-level information, even in the presence of a modality gap between single-cell and histology data, demonstrates the robustness and versatility of our framework.

4.2. Evaluation on Patch-Level Estimation

Experimental Setup and Datasets. Data preprocessing followed the protocol described in [6]. We used three spatial

Table 3. Comparison of methods across CSCC, Her2st, and STNet datasets. Each (+digit or -digit) shows the difference from the baseline

Method	Ref.	CSCC [15]		Her2st [3]		STNet [13]	
		PCC	SCC	PCC	SCC	PCC	SCC
BLEEP [43]	NeurIPS 2023	-0.0050	-0.0024	0.0212	0.0321	-0.0051	-0.0062
EGN [45]	WACV 2023	0.0552	0.1340	0.0941	0.0479	0.0570	0.0272
STNet [13]	Nat. Biomed.	0.0856	0.1156	0.0849	0.0772	0.0514	0.0536
w/ Ours	Eng. 2020	0.1008 (+0.0152)	0.1662 (+0.0506)	0.0825 (-0.0024)	0.1111 (+0.0339)	0.0532 (+0.0018)	0.0623 (+0.0087)
TRIPLEX [6]	CVPR 2024	0.0895	0.1239	0.0900	0.0861	0.0606	0.0546
w/ Ours		0.1116 (+0.0221)	0.1821 (+0.0582)	0.0865 (-0.0035)	0.1194 (+0.0333)	0.0523 (-0.0083)	0.0621 (+0.0075)

transcriptomics datasets: a cutaneous squamous cell carcinoma (CSCC) dataset [15] and two breast cancer datasets, Her2st [3] and STNet [13]. The CSCC dataset includes both single-cell and spatial transcriptomics modalities; the corresponding single-cell data were obtained from GSE144240 [15]. For Her2st and STNet, we used the GSE176078 dataset [41], which was also used in the BRCA experiments. Unlike prior implementations, we excluded spatial smoothing, as it may introduce bias in downstream analyses [9]. Target genes were selected using the same procedure used for slide-level estimation: after filtering both single-cell and ST data, only genes shared across the two modalities were retained. This resulted in 10,118 genes for CSCC, 9,279 for Her2st, and 7,716 for STNet. For each dataset, model training was performed using patient-level leave-one-out cross-validation to ensure robust subject-level evaluation.

Comparisons on Patch-Level Estimation. We compared our method with four representative benchmarks: **BLEEP** [43], which employs multimodal contrastive learning for gene expression prediction; **EGN** [45], which introduces an exemplar-guided estimation strategy; **STNet** [13], which fine-tunes DenseNet-121 with a linear regression head; and **TRIPLEX** [6], which uses a multi-scale feature aggregation framework. Our method can be integrated into feature-extraction-based models by replacing their feature extractor f_f . To demonstrate this flexibility, we incorporated CPNN into STNet and TRIPLEX and evaluated their performance using the same training protocol.

Table 3 summarizes the results. Integrating CPNN consistently improved SCC performance across all datasets, with the largest gain observed on the CSCC dataset. Because the CSCC dataset contains matched single-cell and spatial transcriptomics data from the same patients, modality alignment is preserved, allowing the prototype information to be utilized more effectively.

Despite the inherent differences in expression scales across modalities, the proposed method maintained comparable PCC while substantially improving SCC. These results indicate that incorporating cell-type prototypes provides meaningful regularization for spatial gene expression prediction, even under multimodal settings, and can en-

Table 4. Ablation study results. PI: prototype initialization of \bar{T} , MC: modality correction using α and β , U: prototype update of \bar{T} , R: regularization loss.

Settings	PI	MC	U	R	SCC
w/o PI, MC, R	✗	✗	✓	✗	0.305
w/o MC, U, R	✓	✗	✗	✗	0.174
w/o U, R	✓	✓	✗	✗	0.248
w/o R	✓	✓	✓	✗	0.336
Ours	✓	✓	✓	✓	0.338

hance the performance of existing patch-level estimation frameworks.

4.3. Ablation Study

Effect of Individual Modules. We assess the module-wise effectiveness of the proposed framework in the slide-level gene expression estimation setting using the BRCA dataset (*i.e.*, an ablation over each model component). Table 4 shows the results of validating each module. PI: prototype-informed, which uses estimated \bar{T} for initial value of prototype, MC: modality correction by α and β , U: whether to update prototype T , and R: using regularization loss. "w/o PI, MC, R" refers to the case where proportion and prototype were trained from scratch with L_{NB} .

The performance of "w/o PI, MC, R" is similar to MOSBY, which takes a summation of the estimated gene expression for each patch. Our findings suggest that without any guidance of prototype and regularization, it shows similar performance to MOSBY and yields no performance gain. The result demonstrates that our prototype-informed approach contributes to improving performance. There are biases between single-cell and bulk data due to multiple factors. Consequently, using a prototype derived from single-cell data without updating it results in performance degradation relative to scratch (w/o MC, U, R). To address the bias between the two data datasets, we introduced modality correction using factors $\bar{\alpha}$ and $\bar{\beta}$, leading to a performance gain (w/o U, R). However, the modality correction alone was insufficient to bridge the modality gap, limiting over-

Table 5. Effect of cell-type label granularity on model performance (SCC).

	Coarse (8)	medium (29)	fine (49)
	0.317	0.336	0.338

all improvement fully. Updating the prototype (“w/o R”) improved performance compared to training from scratch, indicating that initializing with our cell-type prototype-informed model enhances generalization. While the regularization term does not lead to significant performance gains, it enforces consistency with the deconvolution results, which in turn preserves the interpretability of the estimated cell-type compositions.

Effect of Cell-Type Label Granularity. Cell-type annotations vary in granularity. For instance, T cells can be subdivided into finer categories such as CD4⁺ T cells and conventional T cells. Single-cell datasets often provide labels at multiple resolutions, and the chosen level of granularity may influence model performance. Coarse labels may obscure biologically meaningful heterogeneity, whereas overly fine-grained labels may produce categories that are not visually distinguishable in histology, resulting in limited performance gains.

To assess the effect of label granularity, we constructed prototypes using BRCA single-cell data under three labeling schemes—coarse, medium, and fine—containing 9, 29, and 49 cell types, respectively. Table 5 summarizes the results in terms of SCC. Overall, the model remained robust across medium and fine levels of granularity, with only minor variations in SCC and PCC. Performance degradation was observed primarily with coarse labels, likely due to the reduced number of prototypes limiting the model’s representational capacity. These results suggest that moderate granularity provides a favorable balance between biological resolution and model flexibility.

Biological Validation of Compositional Weights. By integrating cell-type prototypes into the model, we obtain not only predicted gene expression values but also the corresponding prototype weights. These weights provide cell-type-level explanations for the predictions, thereby enhancing interpretability. To evaluate whether the estimated compositional weights are biologically meaningful, we analyzed the BRCA dataset and examined the prototype weights predicted for each whole-slide image. We focused on cancer-related prototypes derived from single-cell data and visualized their average weights across slides.

Figure 4 shows the average weights predicted by CPNN for each BRCA subtype. In addition to the subtype-associated prototypes, we also visualize the Cycling prototype, which represents proliferative tumor programs and is informative for distinguishing tumor aggressiveness.

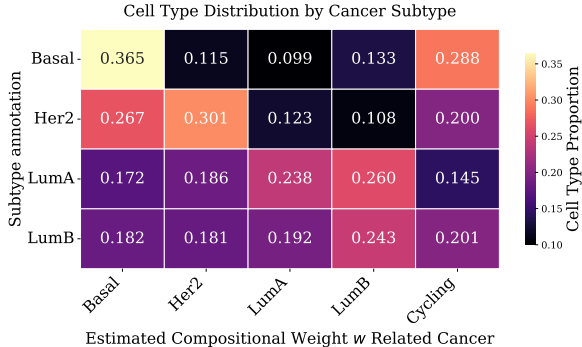


Figure 4. Average weight for each subtype of BRCA slides. We visualized the estimated weights for the cancer-related prototypes.

First, focusing on the subtype-specific prototypes (excluding Cycling), we find that each subtype exhibits a high probability for the compositional weight corresponding to its expected cell-type program. Despite the absence of subtype supervision during training, the model assigns higher weights to prototypes that align with known BRCA subtype characteristics. In LumA tumors, both LumA and LumB prototypes show similar activation levels. This observation is consistent with previous studies [41] and likely reflects the similar expression profiles shared by these two subtypes. The Cycling prototype receives the highest weights in Basal-like tumors, consistent with their highly proliferative phenotype. Cycling weights are also higher in LumB tumors than in LumA tumors, reflecting the greater proliferative activity known for LumB.

Collectively, these results demonstrate that the inferred compositional weights reveal which cell types drive the predicted expression patterns, thereby providing clear and biologically grounded interpretability.

5. Conclusion

In this paper, we proposed a Cell-type Prototype-informed Neural Network (CPNN) for gene expression estimation from whole-slide images. To leverage cell-level datasets despite their modality gap and severe noise, we introduced cell-type prototypes, which represent stable gene expression profiles for each cell type. Across three slide-level and three patch-level datasets, CPNN consistently outperformed existing methods, demonstrating its robustness and general applicability. Moreover, the prototype decomposition provides interpretable cell-type contributions, offering biologically meaningful insights that cannot be obtained through conventional feature-based approaches. These results suggest that incorporating cell-level information through cell-type prototypes is a promising direction for improving both accuracy and interpretability in computational gene expression prediction.

Acknowledgment

Funding in direct support of this work: JSPS KAKEN JP24KJ2205, 23H03862, and JP23K16991, JST ACT-X JPMJAX23CR, JST ASPIRE JPMJAP2403, AMED grant JP24ama221609h0001(P-PROMOTE) (to YK) and JP25gm7010014h0001(PRIME), National Cancer Center Research and Development Fund 2024-A-6 (to YK). We used ABCI 3.0 provided by AIST and AIST Solutions.

References

- [1] Imad Eldin Ali Abugessaisa, Shuhei Noguchi, Michael Böttcher, Akira Hasegawa, Tsukasa Kouno, Sachi Kato, Yuhki Tada, Hiroki Ura, Kuniya Abe, Jay W. Shin, Charles Plessy, Piero Carninci, and Takeya Kasukawa. SCPortalen: human and mouse single-cell centric database. *Nucleic Acids Res.*, 46:D781–D787, 2017. 2
- [2] Areej Alsaafin, Amir Safarpour, Milad Sikaroudi, Jason D. Hipp, and Hamid R. Tizhoosh. Learning to predict RNA sequence expressions from whole slide images with applications for search and classification. *Commun. Biol.*, 6, 2022. 1, 2, 6
- [3] Alma Andersson, Ludvig Larsson, Linnea Stenbeck, Fredrik Salmén, Anna Ehinger, Sunny Wu, Ghamdan Al-Eryani, Daniel Roden, Alex Swarbrick, Åke Borg, et al. Spatial deconvolution of HER2-positive breast tumors reveals novel intercellular relationships. *bioRxiv*, pages 2020–07, 2020. 7
- [4] Tanya Barrett, Stephen E Wilhite, Pierre Ledoux, Carlos Evangelista, Irene F Kim, Maxim Tomashevsky, Kimberly A Marshall, Katherine H Phillippy, Patti M Sherman, Michelle Holko, et al. NCBI GEO: archive for functional genomics data sets—update. *Nucleic Acids Res.*, 41(D1):D991–D995, 2012. 2
- [5] Tinyi Chu, Zhong Wang, Dana Pe’er, and Charles G Danko. Cell type and gene expression deconvolution with BayesPrism enables Bayesian integrative analysis across bulk and single-cell RNA sequencing in oncology. *Nat. Cancer*, 3(4):505–517, 2022. 2
- [6] Youngmin Chung, Ji Hun Ha, Kyeong Chan Im, and Joo Sang Lee. Accurate spatial gene expression prediction by integrating multi-resolution features. In *CVPR*, pages 11591–11600, 2024. 1, 2, 6, 7
- [7] Thao M Dang, Haiqing Li, Yuzhi Guo, Hehuan Ma, Feng Jiang, Yuwei Miao, Qifeng Zhou, Jean Gao, and Junzhou Huang. Hage: Hierarchical alignment gene-enhanced pathology representation learning with spatial transcriptomics. In *MICCAI*, pages 228–238. Springer, 2025. 2
- [8] Leo Fillioux, Joseph Boyd, Maria Vakalopoulou, Paul-Henry Cournède, and Stergios Christodoulidis. Structured state space models for multiple instance learning in digital pathology. In *MICCAI*, pages 594–604. Springer, 2023. 3, 6
- [9] Aniruddha Ganguly et al. MERGE: Multi-faceted Hierarchical Graph-based GNN for Gene Expression Prediction from Whole Slide Histopathology Images. In *CVPR*, pages 15611–15620, 2025. 2, 7
- [10] Mara Graziani, Niccolò Marini, Nicolas Deutschmann, Nikita Janakarajan, Henning Müller, and María Rodríguez-Martínez. Attention-based interpretable regression of gene expression in histology. In *MICCAIW*, pages 44–60. Springer, 2022. 1, 2, 6
- [11] Artur Gynter, Dimitri Meistermann, Harri Lähdesmäki, and Helena Kilpinen. DeconV: Probabilistic Cell Type Deconvolution from Bulk RNA-sequencing Data. *bioRxiv*, pages 2023–12, 2023. 2
- [12] Haviv et al. The covariance environment defines cellular niches for spatial inference. *Nature Biotechnology*, 43(2): 269–280, 2025. 1
- [13] Bryan He, Ludvig Bergensträhle, Linnea Stenbeck, Abubakar Abid, Alma Andersson, Åke Borg, Jonas Maaskola, Joakim Lundberg, and James Zou. Integrating spatial gene expression and breast tumour morphology via deep learning. *Nat. Biomed. Eng.*, 4(8):827–834, 2020. 1, 2, 7
- [14] Maximilian Ilse, Jakub Tomczak, and Max Welling. Attention-based deep multiple instance learning. In *ICML*, pages 2127–2136. PMLR, 2018. 3, 6
- [15] Andrew L Ji, Adam J Rubin, Kim Thrane, Sizun Jiang, David L Reynolds, Robin M Meyers, Margaret G Guo, Benson M George, Annelie Mollbrink, Joseph Bergensträhle, et al. Multimodal analysis of composition and spatial architecture in human squamous cell carcinoma. *cell*, 182(2): 497–514, 2020. 7
- [16] Yuran Jia, Junliang Liu, Li Chen, Tianyi Zhao, and Yadong Wang. THitoGene: a deep learning method for predicting spatial transcriptomics from histological images. *Briefings in Bioinformatics*, 25(1), 2023. 2
- [17] Hyeontae Jo, Hyukpyo Hong, Hyung Ju Hwang, Won Chang, and Jae Kyoung Kim. Density physics-informed neural networks reveal sources of cell heterogeneity in signal transduction. *Patterns*, 5(2), 2024. 3
- [18] Dragomirka Jovic, Xue Liang, Hua Zeng, Lin Lin, Fengping Xu, and Yonglun Luo. Single-cell RNA sequencing technologies and applications: A brief overview. *Clin. Transl. Med.*, 12(3):e694, 2022. 3
- [19] Ali Kamali, Mohammad Sarabian, and Kaveh Laksari. Elasticity imaging using physics-informed neural networks: Spatial discovery of elastic modulus and poisson’s ratio. *Acta Biomater.*, 155:400–409, 2023. 2
- [20] Nayoung Kim, Hong Kwan Kim, Kyungjong Lee, Yourae Hong, Jong Ho Cho, Jung Won Choi, Jung-Il Lee, Yeon-Lim Suh, Bo Mi Ku, Hye Hyeon Eum, et al. Single-cell RNA sequencing demonstrates the molecular and cellular reprogramming of metastatic lung adenocarcinoma. *Nat. Commun.*, 11(1):2285, 2020. 6, 2
- [21] Vitalii Kleshchevnikov, Artem Shmatko, Emma Dann, Alexander Aivazidis, Hamish W King, Tong Li, Rasa Elementaite, Artem Lomakin, Veronika Kedlian, Adam Gayoso, et al. Cell2location maps fine-grained cell types in spatial transcriptomics. *Nat. Biotechnol.*, 40(5):661–671, 2022. 4, 5, 1
- [22] Yasuhiro Kojima, Shinji Mii, Shuto Hayashi, Haruka Hirose, Masato Ishikawa, Masashi Akiyama, Atsushi Enomoto, and Teppei Shimamura. Single-cell colocalization analysis using a deep generative model. *Cell Systems*, 15(2):180–192, 2024. 2

- [23] Ruoyan Li, John R Ferdinand, Kevin W Loudon, Georgina S Bowyer, Sean Laidlaw, Francesc Muiyas, Lira Mamanova, Joana B Neves, Liam Bolt, Eirini S Fasouli, et al. Mapping single-cell transcriptomes in the intra-tumoral and associated territories of kidney cancer. *Cancer cell*, 40(12):1583–1599, 2022. 6, 2
- [24] Haotian Liu, Chunyuan Li, Yuheng Li, and Yong Jae Lee. Improved baselines with visual instruction tuning. In *CVPR*, pages 26296–26306, 2024. 5
- [25] Romain Lopez, Jeffrey Regier, Michael B Cole, Michael I Jordan, and Nir Yosef. Deep generative modeling for single-cell transcriptomics. *Nat. Methods*, 15(12):1053–1058, 2018. 4
- [26] Ilya Loshchilov and Frank Hutter. Decoupled weight decay regularization. In *ICLR*, 2019. 5
- [27] Michael I Love, Wolfgang Huber, and Simon Anders. Moderated estimation of fold change and dispersion for RNA-seq data with DESeq2. *Genome biology*, 15:1–21, 2014. 5
- [28] Ming Y Lu, Drew FK Williamson, Tiffany Y Chen, Richard J Chen, Matteo Barbieri, and Faisal Mahmood. Data-efficient and weakly supervised computational pathology on whole-slide images. *Nat. Biomed. Eng.*, 5(6):555–570, 2021. 4, 5
- [29] Ming Y Lu, Bowen Chen, Drew FK Williamson, Richard J Chen, Ivy Liang, Tong Ding, Guillaume Jaume, Igor Odintsov, Long Phi Le, Georg Gerber, et al. A visual-language foundation model for computational pathology. *Nat. Med.*, 30(3):863–874, 2024. 5
- [30] Vivien Marx. Method of the Year: spatially resolved transcriptomics. *Nat. Methods*, 18(1):9–14, 2021. 3
- [31] Ali Mortazavi, Brian A Williams, Kenneth McCue, Lorian Schaeffer, and Barbara Wold. Mapping and quantifying mammalian transcriptomes by RNA-Seq. *Nat. methods*, 5(7):621–628, 2008. 3
- [32] ICGC/TCGA Pan-Cancer Analysis of Whole Genomes Consortium. Pan-cancer analysis of whole genomes. *Nature*, 578(7793):82–93, 2020. 2
- [33] Minxing Pang, Kenong Su, and Mingyao Li. Leveraging information in spatial transcriptomics to predict super-resolution gene expression from histology images in tumors. *BioRxiv*, pages 2021–11, 2021. 1, 2
- [34] Marija Pizurica, Yuanning Zheng, Francisco Carrillo-Perez, Humaira Noor, Wei Yao, Christian Wohlfart, Antoaneta Vladimirova, Kathleen Marchal, and Olivier Gevaert. Digital profiling of gene expression from histology images with linearized attention. *Nat. Commun.*, 15(1):9886, 2024. 1, 2, 6
- [35] Benoît Schmauch, Alberto Romagnoni, Elodie Pronier, Charlie Saillard, Pascale Maillé, Julien Calderaro, Aurélie Kamoun, Meriem Sefta, Sylvain Toldo, Mikhail Zaslavskiy, et al. A deep learning model to predict rna-seq expression of tumours from whole slide images. *Nat. Commun.*, 11(1):3877, 2020. 2, 6
- [36] Yasin Şenbabaoğlu, Vignesh Prabhakar, Aminollah Khorramali, Jeff Eastham, Evan Liu, Elisa Warner, Barzin Nabet, Minu Srivastava, Marcus Ballinger, and Kai Liu. MOSBY enables multi-omic inference and spatial biomarker discovery from whole slide images. *Sci. Rep.*, 14(1):18271, 2024. 1, 2, 6
- [37] Leyla Tarhan, Jonathan Bistline, Jean Chang, Bryan Galoway, Emily Hanna, and Eric M. Weitz. Single Cell Portal: an interactive home for single-cell genomics data. *bioRxiv*, 2023. 2
- [38] Juan Diego Toscano, Vivek Oommen, Alan John Varghese, Zongren Zou, Nazanin Ahmadi Daryakenari, Chenxi Wu, and George Em Karniadakis. From pinns to pikans: Recent advances in physics-informed machine learning. *arXiv preprint arXiv:2410.13228*, 2024. 2
- [39] Xinggang Wang, Yongluan Yan, Peng Tang, Xiang Bai, and Wenyu Liu. Revisiting multiple instance neural networks. *Nat. Med. Pattern Recognit.*, 74:15–24, 2018. 3, 6
- [40] Xuran Wang, Jihwan Park, Katalin Susztak, Nancy R Zhang, and Mingyao Li. Bulk tissue cell type deconvolution with multi-subject single-cell expression reference. *Nat. Commun.*, 10(1):380, 2019. 2
- [41] Sunny Z Wu, Ghamdan Al-Eryani, Daniel Lee Roden, Simon Junankar, Kate Harvey, Alma Andersson, Aatish Thennavan, Chenfei Wang, James R Torpy, Nenad Bartonicek, et al. A single-cell and spatially resolved atlas of human breast cancers. *Nature genetics*, 53(9):1334–1347, 2021. 6, 7, 8, 2
- [42] Jinxi Xiang and Jun Zhang. Exploring low-rank property in multiple instance learning for whole slide image classification. In *ICLR*, 2023. 3, 6
- [43] Ronald Xie, Kuan Pang, Sai Chung, Catia Perciani, Sonya MacParland, Bo Wang, and Gary Bader. Spatially resolved gene expression prediction from histology images via bi-modal contrastive learning. *NeurIPS*, 36:70626–70637, 2023. 2, 7
- [44] Shu Yang, Yihui Wang, and Hao Chen. MambaMIL: Enhancing long sequence modeling with sequence reordering in computational pathology. In *MICCAI*, pages 296–306. Springer, 2024. 3, 6
- [45] Yan Yang, Md Zakir Hossain, Eric A Stone, and Shafin Rahman. Exemplar guided deep neural network for spatial transcriptomics analysis of gene expression prediction. In *WACV*, pages 5039–5048, 2023. 1, 2, 7
- [46] Yuki Yasuda, Ryo Onishi, Yuichi Hirokawa, Dmitry Kolomenskiy, and Daisuke Sugiyama. Super-resolution of near-surface temperature utilizing physical quantities for real-time prediction of urban micrometeorology. *Building and Environment*, 209:108597, 2022. 2
- [47] Yuansong Zeng, Zhuoyi Wei, Weijiang Yu, Rui Yin, Yuchen Yuan, Bingling Li, Zhonghui Tang, Yutong Lu, and Yuedong Yang. Spatial transcriptomics prediction from histology jointly through transformer and graph neural networks. *Brief. Bioinform.*, 23(5):bbac297, 2022. 1, 2
- [48] Jingwei Zhang, Anh Tien Nguyen, Xi Han, Vincent Quoc-Huy Trinh, Hong Qin, Dimitris Samaras, and Mahdi S Hosseini. 2dMamba: Efficient state space model for image representation with applications on giga-pixel whole slide image classification. In *CVPR*, pages 3583–3592, 2025. 3, 6
- [49] Yuanning Zheng, Marija Pizurica, Francisco Carrillo-Perez, Humaira Noor, Wei Yao, Christian Wohlfart, Kathleen Marchal, Antoaneta Vladimirova, and Olivier Gevaert. Dig-

ital profiling of cancer transcriptomes from histology images with grouped vision attention. *bioRxiv*, pages 2023–09, 2024. [1](#)

Cell-Type Prototype-Informed Neural Network for Gene Expression Estimation from Pathology Images

Supplementary Material

6. Additional discussion on the motivation.

The main text briefly describes the motivation for using single-cell RNA sequencing (scRNA-seq) as a reference modality for spatial transcriptomics (ST) integration. Here, we provide additional background and discussion to complement that description.

Recent advances in high-resolution spatial transcriptomics technologies, such as Xenium, have enabled spatial profiling at near single-cell resolution. However, despite these technological developments, scRNA-seq remains a more robust and scalable reference modality due to its whole-transcriptome coverage and the widespread availability of large-scale datasets [12].

Existing cell-resolved ST platforms are typically constrained by targeted gene panels and high sparsity. In many cases, only a few hundred genes are measured per cell (e.g., around 300 genes), whereas scRNA-seq experiments commonly capture several thousand genes per cell (often around 5,000). As a result, scRNA-seq generally provides higher RNA capture efficiency and more comprehensive transcriptomic coverage.

Because of these limitations, many practical analyses in spatial transcriptomics are performed at the slide or patch level rather than strictly at the single-cell resolution. These settings remain among the most common analysis scenarios in current studies.

In this context, leveraging scRNA-seq as a prior provides a promising direction for scalable integration across transcriptomic modalities. By utilizing the rich transcriptomic information available from scRNA-seq, it becomes possible to guide the analysis of spatial data and facilitate the integration of bulk RNA-seq and spatial transcriptomics data in a scalable and robust manner.

7. Derivation of the Negative Binomial Negative Log-Likelihood

In the main text, we formulate the training objective as the sum of the negative log-likelihood of the assumed data distribution (L_{NB}) and a regularization term. In this section, we derive the negative log-likelihood function associated with the negative binomial model L_{NB} . The motivation of using of negative binomial distribution is to deal with over dispersion problem with count data similar to [21]. We assume that a set of observed bulk $\mathbf{E}^b = \{e_g^{b(n)}\}_{n=1}^{N_m}$, where $e_g^{b(n)}$ denotest each observed bulk gene expression count for gene g in slide n . The set of predicted mean

$\bar{\mu}^b = \{\bar{\mu}^b(\mathcal{X}^{(n)})\}_{n=1}^{N_m}$ and dispersion $\theta^b \in \mathbb{R}^{N_g}$. The negative log-likelihood over a mini-batch of N_m slides is therefore written as

$$L_{\text{NB}}(\mathbf{E}^b, \bar{\mu}^b, \theta^b) = -\frac{1}{N_m} \sum_{n=1}^{N_m} \sum_{g=1}^{N_g} \log \Pr(e_g^{b(n)} | \mathcal{X}^{(n)}). \quad (9)$$

Using the probability mass function of the negative binomial distribution,

$$\Pr(k | \mu, \theta) = \frac{\Gamma(k + \theta)}{\Gamma(\theta) \Gamma(k + 1)} \left(\frac{\mu}{\mu + \theta}\right)^k \left(\frac{\theta}{\mu + \theta}\right)^\theta, \quad (10)$$

the log-probability decomposes into a sum of Gamma-function terms and logarithmic terms involving the mean and dispersion. Substituting this expression into the definition of L_{NB} yields

$$\begin{aligned} L_{\text{NB}} = & -\frac{1}{N_m} \sum_{n=1}^{N_m} \sum_{g=1}^{N_g} \left[\log \Gamma(e_g^{b(n)} + \theta_g^b) - \log \Gamma(\theta_g^b) \right. \\ & - \log \Gamma(e_g^{b(n)} + 1) + e_g^{b(n)} \log \left(\frac{\bar{\mu}_g^b(\mathcal{X}^{(n)})}{\theta_g^b + \bar{\mu}_g^b(\mathcal{X}^{(n)})} \right) \\ & \left. + \theta_g^b \log \left(\frac{\theta_g^b}{\theta_g^b + \bar{\mu}_g^b(\mathcal{X}^{(n)})} \right) \right]. \quad (11) \end{aligned}$$

Here, $\Gamma(\cdot)$ denotes the Gamma function, and the dispersion parameter θ_g^b controls the degree of overdispersion relative to a Poisson model. The first three terms arise from the combinatorial normalization constant of the negative binomial distribution, while the last two terms correspond to the contributions from the mean-dependent success and failure probabilities.

8. Processing Detail of Dataset

To assess the effectiveness of the proposed method, we validated our approach using three publicly available datasets from TCGA: BRCA, KIRC, and LUAD. To collect the bulk dataset, we first matched gene expression data with corresponding pathology images based on sample IDs. Next, we filtered out low-quality samples in which mitochondrial gene expression exceeded 30%, as these samples may indicate cellular stress. Additionally, we removed samples exhibiting abnormally high expression levels exceeding 40,000 counts. We included only samples expressing

more than 5,000 genes and genes detected in at least 50 samples. To obtain the single-cell dataset, we prepared sufficiently large datasets for each organ. Filtering was performed similarly to the bulk dataset, selecting only cells in which mitochondrial gene expression was below 30%. Additionally, samples with gene expression exceeding 2,500 were filtered out. We used only cells that expressed at least 200 genes and genes that were expressed in at least 200 cells.

BRCA: We collected 1,575 whole-slide images (WSI) and gene expression pairs from primary cases in the TCGA-BRCA cohort, encompassing 51,752 genes. After filtering, we obtained 1,474 paired samples encompassing 36,739 genes. We used processed GSE176078[41] which contains 100,064 cells encompassing 29,733 genes. 77839 cells encompassing 15621 genes are extracted by filtering. We used the 14,047 genes common to both bulk and single-cell as the target genes for estimation. The canonical lineage markers were used for cell-type annotation, and 49 cell-type labels were assigned for each cell.

KIRC: We collected 1,081 whole-slide images (WSI) and gene expression pairs from primary cases in the TCGA-KIRC cohort encompassing 49,873 genes. After filtering, we obtained 681 paired samples encompassing 30,723 genes. We used RCC dataset [23] which contains 270,855 cells encompassing 19736 genes. 265825 cells encompassing 16395 genes are extracted by filtering. We used the 14,300 genes common to both bulk and single-cell as the target genes for estimation. Annotation is added based on clustering, and 106 cell-type labels are assigned.

LUAD: We collected 809 whole-slide image (WSI) and gene expression pairs from primary cases in the TCGA-LUAD cohort encompassing 49,093 genes. After filtering, we obtained 756 paired samples encompassing 31,036 genes. We used dataset [20] which contains 208,506 cells encompassing 29,634 genes. 171,128 cells encompassing 16,619 genes are extracted by filtering. We used the 14,520 genes common to both bulk and single-cell as the target genes for estimation.

9. Ablation Study on Prototype Construction

To evaluate the importance of cell-type prototypes, we compare our approach with a non-cell-type baseline constructed by clustering raw gene expression profiles. Due to strong batch effects in the data, this baseline fails to recover meaningful cell-type partitions.

We generate prototypes using 10, 40, and 70 clusters and evaluate their performance (Table 6). The resulting SCC scores are 0.297 (−0.041), 0.300 (−0.038), and 0.303 (−0.035), respectively, showing no improvement over random initialization.

We further compare our method with a simple prototype construction based on averaging gene expression profiles

(Average prototype). This averaging approach achieves an SCC of 0.329 (−0.009), which remains inferior to the proposed prototype formulation.

We also examine a variant without the α and β parameters. Although a similar optimization can still be achieved (SCC: 0.331 (−0.007)), these parameters help disentangle global scale and bias effects from cell-type-specific variations. This contributes not only to improved performance but also to better interpretability of the model. In practice, although this assessment is qualitative, the estimated cell-type proportions obtained without MC appear degraded compared with those obtained with MC.

Table 6. Comparison of prototype construction strategies. SCC values are reported, with performance differences from the proposed method shown in parentheses.

Method	Setting	SCC
Baseline	10 clusters	0.297 (-0.041)
Baseline	40 clusters	0.300 (-0.038)
Baseline	70 clusters	0.303 (-0.035)
Average prototype	–	0.329 (-0.009)
w/o α and β	–	0.331 (-0.007)
Ours	cell-type informed	0.338

10. Examples of cell-type proportion estimation

We utilized BRCA subtype annotations from the cBioPortal dataset [32] and confirmed example of estimation for each subtypes. Leveraging single-cell annotations, the cancer-related compositional weights can be intuitively visualized. Figure 5 shows examples of the estimated cell-type proportions for cancer-related subtype. The results indicate that subtype-specific cell types are accurately identified with high proportions, demonstrating that the prototype effectively leverages subtype-specific gene expression.

Because gene expression profiles are inherently high-dimensional, it is difficult to directly validate predictions using only the estimated expression values. The proposed interpretability therefore provides a valuable means to assess the estimation validity and holds promise for improving the reliability of predictions through comparison with pathologists’ observations. Furthermore, integrating our framework with cell segmentation could enhance both interpretability and predictive performance by modeling the spatial distribution of tumor subtypes, and extending it to jointly incorporate slide- and patch-level estimations may enable spatially resolved interpretability in gene expression prediction.

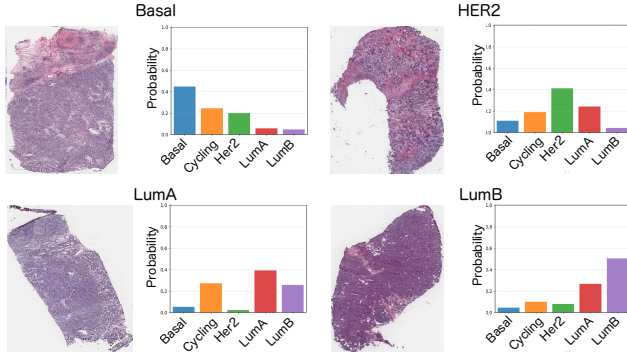


Figure 5. Example of estimated proportion.

BRCA	KIRC	LUAD
0.338	0.370	0.253

Table 7. Deconvolution result of cell2location.

11. Discussion about Cell-level Prototype

If the correct cell-level prototype can be accurately derived from cell-level gene expression data, keeping the prototype fixed would enhance interpretability and preserve gene-gene covariance relationships. However, as demonstrated in our results with fixed prototypes of w/o U in Table 2, factors such as the modality gap, experimental condition gap, and observational noise make it difficult to use prototypes without updates.

Figure 6 shows the parameter distribution of the prototype on BRCA. Each subfigure indicates each cell-type prototype. As shown in Figure 6, the proposed method adaptively adjusts prototypes based on cell type. Since some cell types are easier to identify from images than others, our approach leverages data-driven prototype updates to improve gene expression estimation.

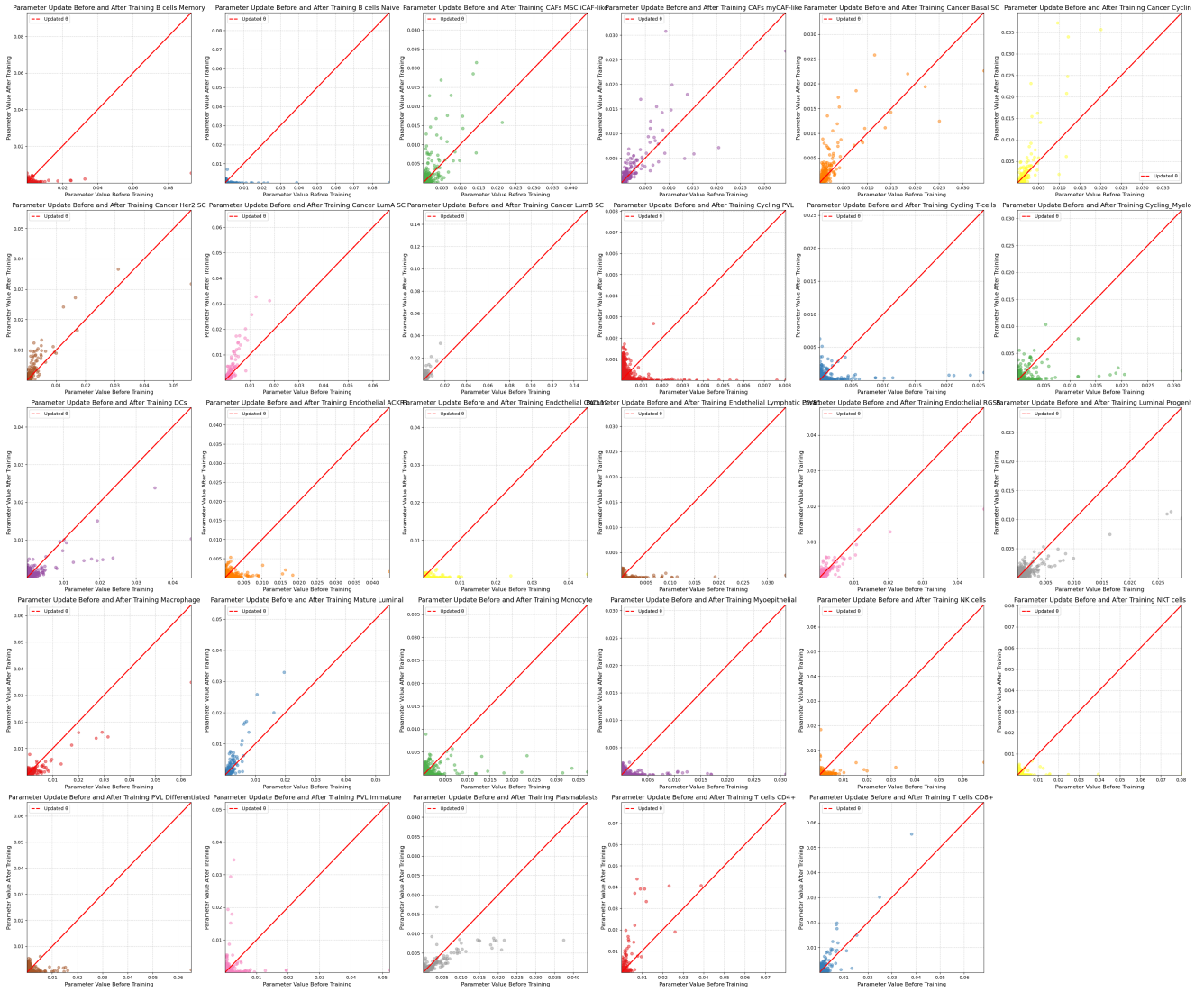


Figure 6. The parameter distribution for cell-type prototype on BRCA before and after training. Each scatter plot corresponds to a specific prototype, with individual points representing genes. The horizontal axis denotes parameter values before training, while the vertical axis represents values after training.